Layered Vanadium Phosphates as Electrodes for Electrochemical Capacitors Part I: The Case of VOPO 4 ×2H 2 O

Jorge Alexis Zúñiga Martínez, Sara Elena González Náñez, Etienne Le Calvez, Raúl Lucio Porto, Iván Eleazar Moreno Cortez, Thierry Brousse, Luis Alberto López Pavón

Layered Vanadium Phosphates as electrodes for Electrochemical Capacitors Part I: The Case of $VOPO_4 \cdot 2H_2O$

Jorge Alexis Zúñiga Martínez[a,b], Sara Elena González Náñez[a,b], Etienne Le Calvez[c,d], Raúl Lucio Porto[a,b,*], Iván Eleazar Moreno Cortez[a,b], Thierry Brousse[c,d], Luis Alberto López Pavón[a,b]

[a] Universidad Autónoma de Nuevo León, Facultad de Ingeniería Mecánica y Eléctrica, San Nicolás de los Garza, 66455, Nuevo León, México
[b] Universidad Autónoma de Nuevo León, Centro de Innovación, Investigación y Desarrollo en Ingeniería y Tecnología, Apodaca, 66600, Nuevo León, México
[c] Université de Nantes, CNRS, Institut des Matériaux Jean Rouxel, IMN, F-44000 Nantes, France
[d] Réseau sur le Stockage Electrochimique de l'Energie (RS2E), CNRS FR 3459, 80039 Amiens Cedex, France

*corresponding author, e-mail: raul.lucioprt@uanl.edu.mx
Phone: +52 (81) 1340-4000 ext 1504

Keywords: Layered Vanadium Phosphate, Electrochemical Capacitors, Supercapacitors, Pseudocapacitance, Ion Intercalation

Abstract

$VOPO_4 \cdot 2H_2O$ was synthesized and investigated as an electrode material for electrochemical capacitors, so-called supercapacitors. The electrochemical characterizations were performed in three different electrolytes (3M $LiNO_3$, 3M KOH and 3M LiOH). Ion intercalation is evidenced by extracting the charge of the double layer, pseudocapacitive and faradaic processes from cyclic voltammograms. It takes place across the entire applied potential window even at scan rates as high as 100 $mV.s^{-1}$. However, as it is depicted and discussed in this study the amount of charge related to each mechanism depends on the nature of the electrolyte. The highest areal capacitance is 500 μFcm^{-2} (70 Fg^{-1}) in 3M LiOH. Moreover, after an initial fade the capacitance stabilizes at 90% of the starting

value after 5000 cycles, thus opening a new use of transition metal phosphates as electrodes for energy storage devices.

1. Introduction

The new upcoming technologies such as electronic devices, electric cars, unmanned aerial vehicles or the internet of things, demand energy storage devices that can grant more power and autonomy. Thus, Electrochemical Capacitors (ECs), so-called supercapacitors, and the related electrode materials have been a popular topic for research upon the last two decades. ECs can store energy through two different mechanisms, a capacitive one related to the accumulation of charges by electrostatic forces in the electrode-electrolyte interface (electrical double layer capacitors, EDLC), and a Faradaic one named pseudocapacitance that store energy due to fast and reversible successive redox reactions at the electrode surface (pseudocapacitive behavior) giving rise to a capacitive-like signature [1-3]. In order to increase the power (rate of charge-discharge) and energy density of ECs, many types of electrode materials have been studied. These include transition metal oxides, metal nitrides, perovskites, redox polymers, MXenes and hybrid materials [1,4-9]. However, inorganic materials such as transition metal phosphates have been poorly studied as electrode materials for ECs. [10,11]

Interestingly, the surface chemistry of transition metal phosphates shows several functional groups as Brønsted (-MOH, -POH) and Lewis (M^{2+}, M^{3+}, M^{4+}, M^{5+}) acids, redox pairs leading to a one or two electrons transfer (M^{5+}/M^{4+}, M^{4+}/ M^{3+}, M^{5+}/ M^{3+}, M^{4+}/M^{2+}), oxygen bridges (M-O-M, M-O-P), and terminal oxygen (P=O, M^{5+}=O, M^{4+}=O) that gives to these materials a wide number of properties for energy storage [12-15]. The presence of such a rich surface chemistry suggests for the

potential use of these materials in ECs. Moreover, some of the crystalline structures exhibit 1D, 2D or 3D tunnels which may play a significant role as pathways for ions transport or ions storage [13,16-19]. The few studies of transition metal phosphates as electrodes for ECs report a large discrepancy between the capacitance values, mainly depending on their chemical composition. For instance, manganese phosphates like $MnPO_4 \cdot H_2O$, $Mn_3(PO_4)_2$ and NH_4MnPO_4 exhibit specific capacitances of 210 Fg^{-1}, 194 Fg^{-1} in KOH and 35 Fg^{-1} in Na_2SO_4 respectively [10,20,21]. Specific capacitance up to 350 Fg^{-1} have been reported for a cobalt phosphate $Co_3(PO_4)_2 \cdot 8H_2O$ with nanoscale pore channels in KOH as electrolyte [22]. Similarly, graphene intercalated with $VOPO_4$ has demonstrated a high specific capacitance of 508 Fg^{-1} in H_2SO_4 [23] and 929 Fcm^{-3} in PVA/LiCl gel electrolyte [24]. However, the charge storage mechanism has not been established for this family of electrode materials, some of them clearly exhibiting a battery like behavior, which has nothing to do with pseudocapacitance. [22,24]

In order to further understand the electrochemical behavior of vanadium phosphates, we report the electrochemical response of $VOPO_4 \bullet 2H_2O$ prepared by a sonication method [25], in three electrolytes (3M $LiNO_3$, 3M KOH and 3M LiOH) and evaluated by cyclic voltammetry and electrochemical impedance spectroscopy in a three electrode cell.

2. Methodology

Synthesis of $VOPO_4 \bullet 2H_2O$

Following the sonication method proposed by Park et. al. [25] an appropriate amount of V_2O_5, (Fermont, 98%), H_3PO_4 (CTR, 85%) and deionized water H_2O were mixed in order to obtain a solution with a fix molar ratio of V_2O_5: H_3PO_4:H_2O = 1 : 50 : 604. The solution was sonicated at 37 kHz during 45 min (Fisherbrand, FB11201, power 120 W). Then the yellow powder was recovered by filtration and washed several times with water and acetone. Finally, the precipitate was dried at room temperature.

2.1 Material Characterization

The X-ray diffraction pattern (XRD) was collected with an Empyrean PANalytical X'Pert Pro diffractometer with an X'Celerator detector and CuK_{α} radiation (λ = 1.5406 Å) operated at 45 kV and 40 mA. The scans were performed in the 2θ range from 5 to 90° with a step scan of 0.02° and 1s per step in a continuous mode. The morphology of the vanadium phosphates was analyzed by scanning electron microscopy (SEM), FEI Nova NanoSEM using a Field Emission Gun and by transmission electron microscopy (TEM), Hitachi H9000-NAR. Infrared spectroscopy (FTIR) analysis was performed on a Thermo Scientific model Nicolet 6700 spectrophotometer. Pellets were prepared with KBr in a weight ratio of 1:50 (sample:KBr). The spectrum was collected with a resolution of 4 cm^{-1} and averaged over 32 scans. The BET surface area was obtained from an Autosorb II.

2.2 Electrochemical Characterization

The electrodes were prepared from a mixture of active material, carbon black and polytetrafluoroethylene (PTFE, Sigma-Aldrich) in a mass ratio of 70:20:10 respectively. Then, the electrode components were mixed with acetone. The paste was cold rolled into a 100 µm thick film and pressed between two stainless steel grids at 1 GPa resulting in active material mass loading of 7 $mg.cm^{-2}$. A three electrode cell was used with a platinum grid as a counter-electrode and an appropriate reference electrode was used, depending on the pH of the electrolyte (Ag/AgCl for neutral pH or Hg/HgO for more basic pH).

The electrochemical measurements were performed using a SP-150 potentiostat-galvanostat (Biologic Instruments). The electrochemical behavior of the electrode material was studied by cyclic voltammetry, chronopotentiometry and

electrochemical impedance spectroscopy (EIS). For the EIS tests, an amplitude of 10 mV was used with a frequency range from 10 mHz to 100 kHz.

The specific capacitance C (F/g) was obtained from Equation 1. Where Q is the charge in C, obtained from the average of integrating the areas of the cyclic voltammogram during oxidation and reduction, ΔV is the width of the electrochemical window in V and m is the mass of active material in grams.

$$C\ (Fg^{-1}) = Q(\Delta V m)^{-1} \quad (1)$$

3. Results

3.1 Material synthesis and characterization

The synthesis of the electrode material involves the dissolution V_2O_5 and precipitation of the vanadium phosphate as described by Park et al. [25], which leads to a yellow powder. Figure 1a shows the diffractogram with well-defined peaks, that indicates the crystalline structure of the material, and it can be indexed to $VOPO_4{\bullet}2H_2O$ (card PDF #36-1472), with tetragonal structure and space group P4/nmm. According to the XRD pattern, there is no evidence of other crystalline phase. This structure has been reported like infinite layers of distorted VO_6 octahedrons united by oxygen bonds to PO_4 tetrahedrons, which alternate each other (see inset in Figure 1). Each vanadium octahedron shares its four equatorial oxygen atoms with four different PO_4 tetrahedrons. One of the remaining axial oxygen consists in the V=O group that alternate up and down relative to the layer (along the [110] direction) with a V-O length of 1.58 Å. The other axial oxygen is also coordinated to a water molecule with a V-O length of 2.58 Å. This implies that the vanadium atom is displaced from the center of the octahedron along the *c* axis. The second water molecule forms hydrogen bonds with two PO_4 groups of different layers. The interlayer distance is 7.40 Å [26-28]. Furthermore, the layers of $VOPO_4$ contains 2D ion transport channels. Thus, upon the reduction of V^{5+} to V^{4+}, cations like H^+, Li^+, Na^+, among others, can be intercalated in the interlayer spacing

[16,23,29,30]; this may increase the charge stored. This is the case for 2D ultrathin vanadyl phosphate nanosheets simulations performed by Peng et. al. [30], where the authors propose a pathway for Na^+ ion migration parallel across the $VOPO_4$ nanosheets.

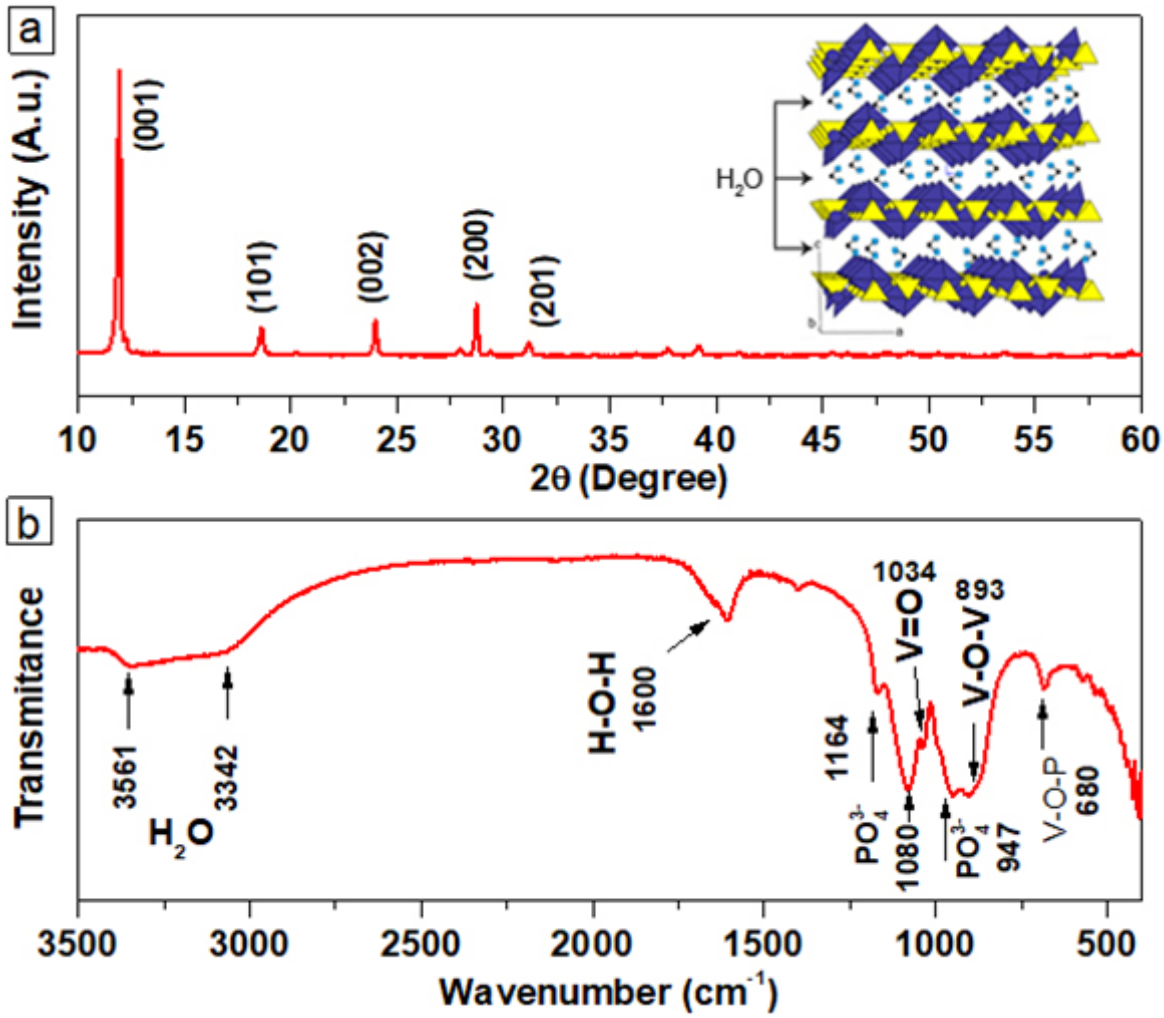

Figure 1. a) XRD patterns and inset crystalline structure of $VOPO_4 \cdot 2H_2O$ (PO_4 tetrahedrons in yellow and VO_6 octahedrons in blue), b) FTIR spectra of $VOPO_4 \cdot 2H_2O$.

Figure 1b shows the FTIR spectroscopy that confirms the formation of vanadium phosphate, as well as the presence of several functional groups including the

stretching vibrations of V-O-P, V=O and P-O_4. The spectrum of $VOPO_4$•$2H_2O$ shows bands located at 680, 893, and 1034 cm^{-1} that corresponds to the bending vibration of V-O-P, the stretching vibration of V-O-V and the stretching vibration of V^{5+}=O respectively [23,31,32]. The bands of PO_4^{3-} group are centered at 947 and 1080 cm^{-1} and can be assigned to asymmetric stretching and the band at 1164 cm^{-1} is due to the stretching vibration [31]. The band at 1600 cm^{-1} is attributed to the stretching vibration of H-O-H [23]. The band at 3342 cm^{-1} can be assigned to the water molecule bound to the V-O group located in the interlayer space [31]. Finally, the band centered at 3561 cm^{-1} corresponds to interlayer free structural water bounded by hydrogen bounds to PO_4 groups [31].

Figure SI1a shows the SEM image of $VOPO_4$•$2H_2O$ that reveals nanoparticles prepared using ultrasonication. The morphology consists in platelets with a 70 nm thickness and particle size around 1.5 µm (Figure SI1a inset, TEM image). Considering the above dimensions, the calculated geometric surface area is close to 14 m^2g^{-1}. The two-dimensional morphology is consistent with the layered crystalline structure. The absorption-desorption isotherm of $VOPO_4$•$2H_2O$ is shown in Figure SI1b. The hysteresis indicates the presence of mesopores with a mean diameter of 15.6 nm. The BET surface area is 14 m^2g^{-1} in agreement with the estimated geometrical surface area.

3.2 Electrochemical characterization

The $VOPO_4$•$2H_2O$ was studied using three different electrolytes (3M KOH, 3M LiOH, and 3M $LiNO_3$) in a three electrode cell in order to evaluate its electrochemical properties. Figure 2a shows the three different electrochemical windows of $VOPO_4$•$2H_2O$ at a scan rate of 5 mVs^{-1}. In alkaline electrolytes, the electrochemical window is 1.0 V and in neutral electrolyte (3M $LiNO_3$) it can be

extended up to 1.1 V. These ranges of potential agree with the reports from literature for aqueous electrolytes [4,24,33,34]. It is worthy to highlight the electrochemical response found from 5 up to 100 mVs^{-1}, that indicates a fast charge-discharge process for $VOPO_4•2H_2O$ in these three electrolytes (see Figure SI2). Typically, the corresponding transition metal oxides like MnO_2 or V_2O_5 usually exhibit a pronounced resistive behavior leading to distorted CVs at fast scan rates as high as 100 mVs^{-1} [34-37] which is not the case for $VOPO_4•2H_2O$ electrode. Additionally, in 3M LiOH a couple of redox peaks are depicted that can be associated to a battery like response at 5 mVs^{-1}. The waves were observed at -0.75 and -0.95 V vs Hg/HgO in the cathodic and anodic sweep, respectively. As the scan rate increase, the cathodic and anodic waves shift to more positive potentials (see Figure SI2a) and the intensity of the waves decrease turning the voltammogram into a rectangular shape. These waves suggest a faradaic charge storage process superimposed to the pseudocapacitive behavior as it was recently reported for $MnPO_4•H_2O$ [10], and other transition metal oxides [34,36,38]. The decreased intensity of the waves at fast scan rate indicates that the faradaic contribution to charge storage is less predominant. In 3M KOH electrolyte a rectangular voltammogram is observed indicating a capacitive-like behavior and the behavior remains even at high scan rates up to 100 mVs^{-1} (see Figure SI2b). The $VOPO_4•2H_2O$ electrode cycled in 3M $LiNO_3$ exhibits a typical pseudocapacitive behavior with a capacitive-like signature, at all scan rates (see Figure SI2c). However, at 0.3 V vs Ag/AgCl a reversible faradaic process arises. [39-41].

Figure 2b shows the specific capacitance of $VOPO_4•2H_2O$ in the three different electrolytes. The maximum specific capacitance values were 70 Fg^{-1}, 60 Fg^{-1}, and 30 Fg^{-1} in 3M LiOH, 3M KOH and 3M $LiNO_3$ respectively. This clearly indicates that a different charge storage process arises when alkaline electrolytes are used. It is well known that the pH of the electrolyte affects the electrochemical behavior of electrochemical capacitors based on vanadium electrodes [33] and other families

of materials [42]. An intercalation ion process in the 2D tunnels is also possible in alkaline electrolytes leading to a higher specific capacitance. Additionally, the higher specific capacitance in 3M LiOH could be related to the lower size of dessolvated Li^+ cation (0.6 Å) with respect to dessolvated K^+ (1.33 Å) that facilitates the intercalation process [43]. However, at scan rates above 25 mVs^{-1}, the specific capacitance in 3M LiOH decreases drastically, around 53 % of its initial value (Figure 2b). Meanwhile the specific capacitance in 3M KOH remains constant. Finally, in the case of 3M $LiNO_3$ the specific capacitance is also constant and there is only a slight decrease above 50 mVs^{-1}.

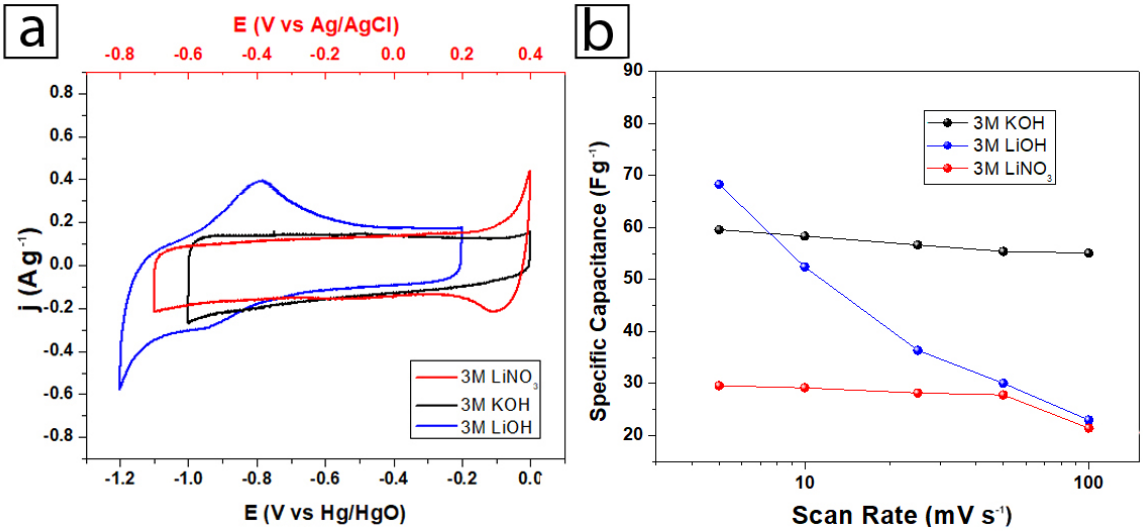

Figure 2. a) Electrochemical windows in different electrolytes at the scan rate of 5 mVs^{-1} and b) Specific capacitance in different electrolytes as a function of the scan rate.

It is a general trend for ECs [4,10,33] that specific capacitance decreases at fast scan rates as it is the case for these vanadium phosphates (see Figure 2b). According to Trasatti et al. [44] only the surface (outer) capacitance is measured at high scan rates, meaning that not all the active sites are reached by the electrolyte ions, especially those that are found in the tunnels of the crystalline structures.

Considering the surface area of $VOPO_4 \cdot 2H_2O$ (14 m^2g^{-1}), the areal capacitance for this material is 500, 430 and 240 μFcm^{-2} in 3M LiOH, 3M KOH and 3M $LiNO_3$. Only in 3M LiOH and 3M KOH the areal capacitances are higher to that of ruthenium oxides [45], metal nitrides [4] or manganese oxides [36] and lower than that reported manganese phosphate [10]. In 3M $LiNO_3$ the areal capacitance is in the range of the reported values shown in Table 1. For an extended comparison table 1 presents the areal capacitances of some reported materials and the vanadium phosphate synthesized in this work. The areal capacitance is a good parameter to compare the performance of different electrode materials with different specific surface areas, since it has been demonstrated that the capacitance will increase with the surface area [4]. Furthermore, a capacitance of 50 μFcm^{-2} can be related to pure double layer since it is in the range of those reported for metals [44,46]. Hence, the areal capacitance of the $VOPO_4 \cdot 2H_2O$ is higher than the maximum double layer capacitance, indicating that charge storage arises from a pseudocapacitive mechanism and in some cases as discussed earlier, from a faradaic process.

Table 1. Areal Capacitances of electrode materials for ECs.

Electrode	Areal capacitance (μFcm^{-2})	Ref
Double Layer Capacitance	50	[44,46]
Ruthenium Oxides	390	[45]
Metal Nitrides	50-300	[4]
Manganese Oxides	110-123	[36]
Manganese Phosphate	1350	[10]
$VOPO_4 \cdot 2H_2O$ in 3M LiOH	500	This work
$VOPO_4 \cdot 2H_2O$ in 3M KOH	430	This work

$VOPO_4 \bullet 2H_2O$ in 3M $LiNO_3$	240	This work

The theoretical specific capacity of $VOPO_4 \bullet 2H_2O$ is 597 Cg^{-1} calculated based upon the insertion of one Li^+ ion per Vanadium cation [47] this value is higher than the 70 Cg^{-1} obtained by cyclic voltammetry in 3M LiOH. Thus, only 12 % of the theoretical capacity is measured. This may suggest that energy storage processes like double layer formation (capacitive), surface successive redox reactions (pseudocapacitive) and faradaic reactions (battery like behavior) only occur near the surface material and not in all the volume of the electrode material as in the case of batteries.

In order to determine the origin of the charge processes of this electrode material, the current density at a fixed potential was obtained from the cyclic voltammograms of the layered vanadium phosphates in 3M LiOH electrolyte. For an ideal capacitor (with only double layer formation), the equation 4 describes the behavior of *i*, which is the current density in function of v, that is the scan rate and *C*, the capacitance which is a constant [10]. This is also the behavior of a pseudocapacitive electrode.

$$i = vC \tag{4}$$

Figure SI3a shows the current densities at different scan rates at fixed potential in the three electrolytes used. The obtained curve of $VOPO_4 \bullet 2H_2O$ is not linear in 3M LiOH and $LiNO_3$ confirming that the charge storage involves more processes than the formation of the electrical double layer or surface pseudocapacitance, possibly ion intercalation (diffuse current), providing a Faradaic behavior. On contrary, in 3M KOH a straight line was obtained indicating an ideal capacitive/pseudocapacitive behavior.

Furthermore, the origin of the stored charge capacitive and faradaic, can be determined by knowing the origin of the current that can be confirmed with equation 5. Where *i* is the current density at a fixed potential, v is the scan rate and *b* is an adjustable parameter at two conditions. When *b = 1* leads to a current proportional to the scan rate, a capacitive or pseudocapactive response, and *b = 0.5* where the current is proportional to the square root of the scan rate, suggesting a diffusion controlled current that in this work could be assigned to a redox intercalation process [48,50]. The *b* parameter can be easily estimated from the slope of log(i) vs log(v) plot.

$$i = av^b \quad (5)$$

Figure SI3b shows the value of *b* parameter for eight different potentials of $VOPO_4 \cdot 2H_2O$ (-1.0, -0.9, -0.8, -0.7, -0.6, -0.5, -0.4, -0.3 V vs Hg/HgO) using 3M LiOH as electrolyte. The *b* parameter is 0.60 at -1.1 V vs Hg/HgO possibly due to a redox intercalation. Then, increases to 0.98 at -1.0 V vs Hg/HgO and decreases to 0.5 at -0.70 V vs Hg/HgO pointing out a redox intercalation process at the same potentials where a pair of redox peaks are depicted in the CV (Figure 2a). Thus, the *b* value remains below 0.80, as the potential turns more positive. This suggest that a diffusive current contributes to the energy storage, possibly by the ion intercalation through 2D tunnels in the crystalline structure, as it was reported for $MnPO_4 \cdot H_2O$ with 1D tunnels [10]. Additionally, the *b* parameter was obtained for 3M KOH, the values of *b* for 3M KOH are closer to 1 in the potential range -0.9 to -0.1 V vs Hg/HgO. This suggests a contribution of both double layer and surface redox reactions (capacitive current) as the main mechanism of energy storage. Furthermore, the *b* parameter was obtained for 3M $LiNO_3$ from -0.6 to 0.3 V vs Ag/AgCl. The values close to 1 suggest a capacitive or pseudocapacitive behavior along the electrochemical window.

It is evidenced that the stored charge involves different mechanisms for this layered vanadium phosphate and that the obtained *b* parameter values are not equal to 0.5 or 1, but lay in this range, suggesting a mixed charge storage process. Thus, in order to discriminate the charge that arise from electric double layer (EDL), pseudocapacitive and faradaic processes, the Trasatti method [51], which involves a relationship of voltammetric charge with sweep rate, and Dunn method [52], which involves a relationship of voltammetric current with a sweep rate at a fixed potential, should be coupled. In the Trasatti method, the total stored charge relies on the outer surface charge attributed to only the electric double layer and the inner charge is attributed to both pseudocapacitive and faradaic process (see equation 6).

$$q_T = q_O + q_i \quad (6)$$

q_O is obtained from the intercept of the linear plot of the voltammetric charge q(V), versus the sweep rate $v^{-1/2}$, when $v \rightarrow \infty$ (see equation 7).

$$q(V) = q_O + C_1 v^{-1/2} \quad (7)$$

The total charge, q_T is obtained from the intercept of the linear plot of $q(V)^{-1}$ versus $v^{1/2}$ when $v \rightarrow 0$ (see equation 8).

$$\frac{1}{q(V)} = \frac{1}{q_T} + C_2 v^{12} \quad (8)$$

Thus, this method allows to estimate the charge that arise from the electric double layer process and the total charge. Subtracting the double layer charge from the total charge leads to the inner charge that could be composed at least by one of the two processes, pseudocapacitive or Faradaic. Then, Dunn method allows to estimate the capacitive charge that involves the electric double layer and pseudocapacitive process and the charge that arise from diffusion-dependent processes like ion intercalation. The capacitive and pseudocapacitive current is proportional to *v*, the scan rate and the diffusion limited current to $v^{1/2}$. Thus, the

current is the combination of the above process as equation 9 shows. The rearrangement in equation 10 allows to estimate the two constants, k_1 from the slope and k_2 from the intercept of the plot $i(V)v^{-1/2}$ versus $v^{1/2}$ at each fixed potential. The origin of the current and thus the origin of the charge can be known at each potential step.

$$i(V) = k_1 v + k_2 v^{1/2} \quad (9)$$

$$\frac{i(V)}{v^{1/2}} = k_1 v^{1/2} + k_2 \quad (10)$$

Finally, the deconvolution of the three charge storage processes can be achieved by subtracting the charge of the electric double layer estimated with the Trasatti method from the capacitive charge obtained with Dunn method (that includes EDL and pseudocapacitive charge). This leads to calculated values of the EDL, pseudocapacitive and Faradaic charge.

Figure 3 shows the deconvoluted charge of $VOPO_4 \cdot 2H_2O$ in three electrolytes at the scan rate of 5 mVs^{-1} across the applied electrochemical window. The larger contribution of the charge stored process in 3M LiOH, is due to the diffusive charge that arise from an ion intercalation process in all the applied potential window (see Figure 3a). The diffusive charge represents 80 % of the stored charge and the accumulated charge by a pseudocapacitive and EDL processes is significantly lower, i.e. only 19 and 1 % respectively (see Figure 3b). Even at the scan rate of 100 mVs^{-1} the diffusive charge represents 47 % of the total stored charge. Thus, even at high scan rates the ion intercalation process is involved in the charge storage process. The peak of stored charge by Faradaic process reaches its maximum at -0.8 V vs Hg/HgO that corresponds to the same peak observed in the cyclic voltammetry experiment (see Figure 2a). Additionally, in the voltage range from -0.5 to -0.2 V vs Hg/HgO the main contributions to the stored charge are due

to pseudocapacitive and diffusive processes despite the rectangular shape of the cyclic voltammogram shown in Figure 2a for $VOPO_4 \cdot 2H_2O$ in 3M LiOH in the same voltage range. Thus, it is obvious that the rectangular shape of the cyclic voltammogram that indicates a capacitor like-behavior arises from the added currents (or charge) from above mentioned processes in such a way that the total current is constant in the applied voltage range. Thus, the reported rectangular shapes of cyclic voltammograms with no waves or peaks cannot discard pseudocapactive or diffusive process. This is exemplified at the scan rate of 100 mVs^{-1} where the shape of the cyclic voltammetry curve is rectangular with small redox waves, a common response of an electrochemical capacitor. Nevertheless, the stored charge involves the three above mentioned processes as is shown in Figure SI4a.

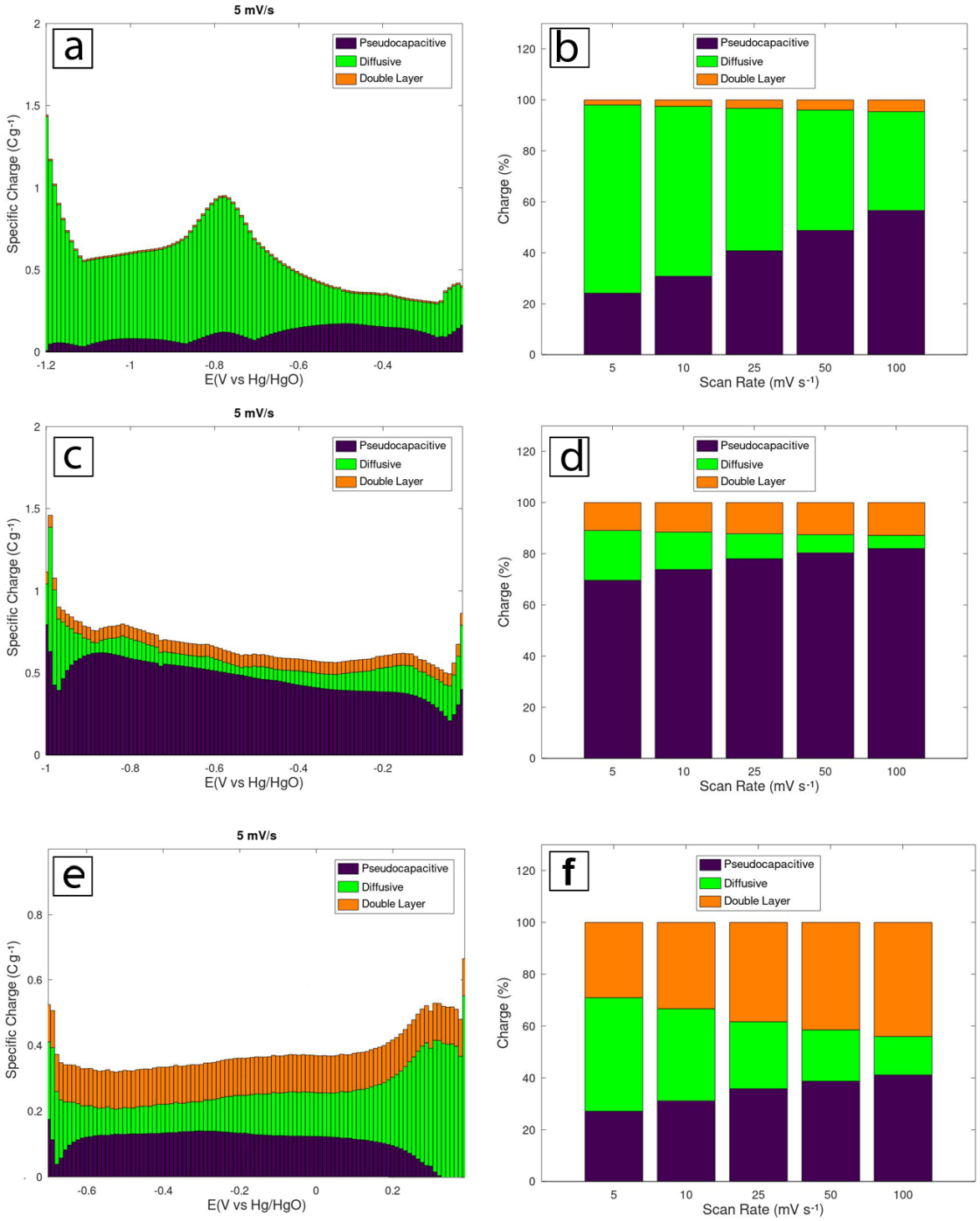

Figure 3. Specific charge of $VOPO_4 \cdot 2H_2O$ originated from EDL, pseudocapacitive and diffusive processes at 5 mVs^{-1} of scan rate in a) 3M LiOH, c) 3M KOH and e) 3M $LiNO_3$ as electrolyte. Percentage of stored charge originated from EDL, pseudocapacitive and

diffusive processes in different scan rate of $VOPO_4 \cdot 2H_2O$ in b) 3M LiOH, d) 3M KOH and f) 3M $LiNO_3$ as electrolyte.

In 3M KOH (Figure 3c) the amount of the pseudocapacitive charge is higher than the diffusive and EDL charge in all applied potential with a peak centered at -0.9 V vs Hg/HgO. Two peaks are observed for the charge arising from a diffusive process centered at -0.8 and -0.2 V vs Hg/HgO. Thus, in a voltage range from -0.6 and -0.4 V vs Hg/HgO the diffusive charge decreases, indicating that dessolvated K^+ ions intercalate-deintercalate towards the more positive and negative potentials of the electrochemical window. However, the shape of the cyclic voltammograms remains rectangular even at the scan rate of 5 mVs^{-1} caused by the pseudocapacitive process that contributes with the higher amount of stored charge (70 %) for 10 % for EDL and 20 % for the diffusive process (see Figure 3d). Thus, this indicates that intercalation of K^+ ions is more difficult compared to Li^+ ion intercalation. This could be caused by the larger size of K^+ ions that would require the removal of water molecules in the interlayer space producing a displacement of the layers and a decrease in the interlayer. These processes could take place at low scan rates, although it seems that at the scan rate of 5 mVs^{-1} or higher, these processes are not carried out or at least not completely. As the scan rate increases, the pseudocapacitive process, remains dominant (see Figure 3d) and the diffusive charge decreases in all the potential window (see Figure SI4b).

Figure 3e shows the charge across the potential window in neutral electrolyte, 3M $LiNO_3$. The three processes are present in all the applied potential. The pseudocapacitive and EDL processes represents the 56 % of the stored charge and a 44 % that arises from a diffusive process (see Figure 3f). In contrast, at the high scan rate of 100 mVs^{-1} the diffusive processes represent only 15 % of the total charge. Thus, the capacitive processes (EDL and pseudocapacitive) govern the stored charge in neutral electrolyte and it is more obvious at 100mVs^{-1} (see Figure

SI4c). This impacts the shape of the voltammograms and leads to a lower specific capacitance than in alkaline media. In summary, the diffusive processes are the main contribution to the stored charge in 3M LiOH. Thus, Li^+ ions intercalate into the 2D tunnels of $VOPO_4•2H_2O$ even at the high scan rate of 100 mVs^{-1} in all the applied potential. In contrast, in 3M KOH and 3M $LiNO_3$ (see Figure 3 d and f) the main contribution to the charge storage are the EDL and the pseudocapacitive processes.

Based on the above-commented data, $VOPO_4•2H_2O$ has a faradaic process with ion insertion in the crystalline structure superimposed to the pseudocapacitive behavior with successive redox reactions and EDL formation in all the applied electrochemical window. The amount of the stored charge from the different processes depends on the nature of the electrolyte. In 3M LiOH the current comes mainly from a process of diffusion due to the intercalation of Li^+ ions in the crystalline structure of $VOPO_4•2H_2O$, between the layers of VO_6 distorted octahedrons vertex united to the tetrahedrons of PO_4 group (inset of Figure 1a) [27,28,52]. Considering the theoretical density of $VOPO_4•2H_2O$ (2.3 gcm^{-3}), a one-electron process and the stored charge versus the applied voltage, the active thickness of the active material particles can be estimated as it is shown in Figure SI5a. Thus, the active thickness of $VOPO_4•2H_2O$ in LiOH is as high as 4.4 nm at -0.8 V vs Hg/HgO where the diffusive current reaches its maximum value. This thickness represents around 7 unitary cells involved in the ion insertion. It is interesting to note that in the voltage range from -0.6 to -0.2 V vs Hg/HgO the active thickness decreases around 1.5 nm leading to only 2.4 unitary cells involved in the ion insertion. In 3M KOH electrolyte, the active thickness is less than 1.0 nm (1.6 unitary cells) in all the applied voltage. Finally, in 3M $LiNO_3$ the active thickness is also less than 1.0 nm, until the voltage range of 0.2 to 0.4 where a faradaic process is evidenced in the cyclic voltammogram (see Figure 2a).

Hence, the particle thickness of $VOPO_4 \cdot 2H_2O$ is 70 nm as mentioned above, this indicates that only 6 % (in 3M LiOH) of their thickness is involved in the charge storage processes. These findings lead to three major remarks:

i) The values of active thickness agree with the previous value reported for $MnPO_4 \cdot H_2O$ (4.5 nm) [10]. It is also important to note that in previous work on vanadium oxynitrides is suggested that the insertion of ions is limited to one unit cell for these materials [4].

ii) The origin of high capacitance of $VOPO_4 \cdot 2H_2O$ in 3M LiOH in terms of gravimetric capacitance (see Figure 2b) or in terms of areal capacitance (see Table 1) despite their poor specific surface area, is related to the large active thickness of these electrode materials. When 3M KOH electrolyte is used, 70 % of the charge arises from pseudocapacitive processes and 10 % from EDL. Only 20 % of the accumulated charge arises from the contribution of the diffusive process. Additionally, the electric double layer and pseudocapacitance are mechanisms that rely on the active surface that in this case is poor (specific surface area 14 m^2g^{-1}), leading to a lower specific capacitance.

iii) These results evidence that the charge-discharge processes do not take place in the bulk electrode material, but at the surface and the subsurface as it is expected for electrochemical capacitors.

Electrochemical Impedance Spectroscopy (EIS) was performed in a frequency range of 10 mHz to 100 kHz at open circuit potential. The Nyquist plot corresponding to $VOPO_4 \cdot 2H_2O$ electrode in three different electrolytes is shown in Figure 4a. A higher value of the electrical series resistance (ESR) is obtained for 3M $LiNO_3$ than in the case of 3M LiOH and 3M KOH, where the ESR value are equal for both alkaline electrolytes (see inset in Figure 4a). This resistance includes the solution resistance, the active material resistance, and electrical contacts resistance. Therefore, as the electrode material is the same in the three

electrolytes and the working electrodes are manufactured in the same way, the low capacitance in 3M $LiNO_3$ is related to its highest ESR. This resistance can originate from the larger size of the hydrated NO_3^- (3.35 Å) anion and lower ionic conductivity than OH^- (3.00 Å) [43]. Furthermore, at higher frequencies a semi-circle is observed in the three different electrolytes (see inset in Figure 4a). The diameter of the semi-circle decreases in the following order $LiNO_3$ > LiOH > KOH. The trend is clear, the larger the hydrated anion size [43] the larger the diameter of the semi-circle. In the case of both alkaline electrolytes the trend follows the size of hydrated cations 3.82 for Li^+ and 3.31 for K^+ ions [43], the larger the hydrated ion size the larger the diameter of the semi-circle. These resistances related to the diameter of the semi-circles are attributed to the electrolyte ions reaching the active surface trough the composite working electrode, in our case, carbon black and PTFE. This behavior was previously reported for electrodes of transition metal oxides and graphite, in which Li^+ ions from electrolyte migrate across a film that cover the surface of active material [53].

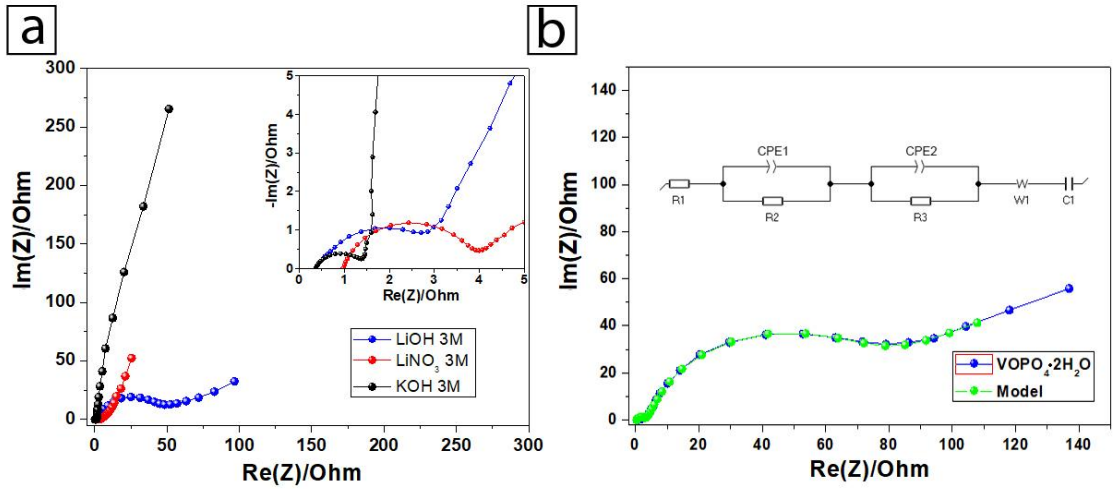

Figure 4. a) Electrochemical impedance spectroscopy of $VOPO_4 \cdot 2H_2O$ at different electrolytes and b) Experimental measured and simulation of circuit model Nyquist plot of $VOPO_4 \cdot 2H_2O$ in 3M LiOH.

In Figure 4a it is shown the middle to low frequencies region of the spectra. When 3M LiOH is used as electrolyte a second semi-circle at high-middle frequencies region is observed. This larger semi-circle is related to the charge transfer resistance (R_{CT}) [54-56]. Moreover, on the low frequency region, a linear correlation between Z_{Im} and Z_{re} which is known as a Warburg type impedance is observed [54-56]. A second semi-circle at high-middle frequencies coupled with a Warburg impedance is typical of an ion intercalation process as it was previously reported on the electrochemical Li^+ ion intercalation in transition metal oxides and graphite and also on Li^+ and Mg^{2+} ion intercalation into Mo_6S_8 [54-58]. Thus, in this case the charge transfer resistance of the second semi-circle is related to the charge transfer of Li^+ ion into the active sites of the electrode material that coupled with the Warburg type impedance indicates the Li^+ ion intercalation. In summary, for $VOPO_4 \cdot 2H_2O$ the techniques of the *b* parameter, the coupled Trasatti-Dunn method and EIS provide evidence for a Li^+ ion intercalation process.

In the case of 3M KOH electrolyte, a diffusion process is also visible by the bended tail at low frequencies, this suggests a diffusion process such as ion intercalation (see Figure 4a) [59]. The intercalation of K^+ ion into the crystalline structure is also evidenced by the coupled Trasatti-Dunn method. However, in 3M KOH the *b* parameter is around 1 and the second semi-circle in the EIS spectrum is not obvious as in the case of 3M LiOH. The reason is that there is a mixed process where the K^+ ion intercalation process take place, however, the surface redox reactions are predominant (see Figure 3c). Furthermore, in 3M $LiNO_3$ electrolyte a straight line is obtained in the low-middle frequencies region that corresponds to the diffusion resistance related to the adsorption of electrolyte ions into the surface-active sites of the electrode material [10], that is a typical pseudocapacitive process. It is worth to mention that the coupled Trasatti-Dunn method indicates a mixed process corresponding to EDL and pseudocapacitive with 56 % of the accumulated charge (see Figure 3e) and the *b* parameter is close to 1.

Finally, at low frequencies the tail is bended towards the real axis (Z_{re}) in 3M LiOH and 3M KOH. This behavior is known as an open boundary finite length Warburg diffusion and is observed when the ion diffusion layer is limited [59]. The origin of this spectrum is that at low frequencies, where the signal of excitation and response of a.c. and d.c techniques approach to each other, the diffusion of the electrolyte ions is limited in such a way that the length of the diffusion layer is comparable in both techniques. Thus, the Z_{im} component becomes less important leading to and increment in Z_{re} (the experimental conditions are close to d.c. excitation), as a result the tail bends towards the real axis. The above leads to two main implications. First, the concentration of the diffusing species is fixed (limited) at one of the boundaries, in this case at the surface of the active material. Second, the fact that Z_{im} becomes less important at low frequencies indicates that despite charge is accumulating, the process is not capacitive in nature, specifically there is not a double layer capacitance or surface successive redox reactions that lead to a pseudocapacitive mechanism, but instead there is an accumulation in the intercalation sites [54-56,59]. Thus, in the case of $VOPO_4 \cdot 2H_2O$ in 3M LiOH, the tail is bended towards the real axis indicating that the diffusion of ions does not come from the bulk of the electrolyte nor trough the components of the composite working electrode, instead it is a Li^+ ion diffusion into the 2D tunnels of the interlayer space. When 3M KOH and $LiNO_3$ electrolytes were used the tails of the spectra are also bent towards the real axis but the extension of these bendings is less predominant, the Z_{im} component becomes more important. This is originated by a mixed process of capacitive (electric double layer and pseudocapacitance) and to a lower extend a diffusive one, as it is indicated by the coupled Trasatti-Dunn method.

For modeling the EIS spectra, an equivalent circuit was chosen based on the several serial processes that take place during the charge storage mechanism of

these materials. Thus, from a phenomenological point of view, the following successive three steps are necessary for the charge storage mechanism. First, electrolyte ion migration through the components of the composite electrode, second a charge transfer in the electro-active material, which originates from the capacitive and pseudocapacitive processes and third an ion intercalation into the tunnels of the crystalline structures (intercalation sites). Then, for the case of 3M LiOH, the model with the equivalent circuit is shown in Figure 4b and is a simplified version based on the work reported by Levi and Aurbach [54]. The R_1 element represent the ohmic resistance of the electrode (resistance of current collector, the active material, and additive materials of electrode fabrication and solution resistance). The simplified Voigt type circuit with a constant phase element (CPE_1) coupled in parallel with R_2 represents the electrolyte ion migration into the active material. Then in series with CPE_2 coupled in parallel with R_3 represents the charge transfer into the active material that leads the capacitive and pseudocapacitive processes. Finally, in series a Frumkin and Melik Gaykazyan impedance, that is Warburg element with a finite diffusion length and an intercalation capacitance C_{int} to model the accumulation in the intercalation sites. The results of the EIS experimental data and the model are displayed in Figure 12. It can be observed that the model fits with the experimental data, indicating that the circuit elements adapted from previous reported works represents the three necessary steps for the charge storage mechanisms described above. Additionally, the Warburg element with a finite diffusion length, it is appropriate to model the intercalation process [59].

Based on the above discussion and in the work reported by Wu and Zhu [24,47], the equation 10 describes the process that may occur during the intercalation of Li^+ ions into the crystalline structure of $VOPO_4 \cdot 2H_2O$, which is the main charge storage mechanism with a process involving the redox couple with one electron transfer, V^V/V^{IV}. However, it is currently not possible to assign a specific redox

reaction to the pseudocapacitive process in 3M LiOH or 3M $LiNO_3$ neutral electrolyte, but it is probably related to the surface electro-adsorption of Li^+ coupled with a redox process of one electron transfer (V^V/V^{IV}). When 3M KOH is used as electrolyte 70 % of the charge arises from a pseudocapacitive process that probably also involves the surface electro-adsorption of K^+ coupled with a redox process of one electron transfer, V^V/V^{IV}. In a similar way, equation 11 shows the process of K^+ ion intercalation.

$$Li^+ + 1e^- + V^VOPO_4 \xrightarrow{\text{Intercalation}} Li\text{-}V^{IV}OPO_4 \quad (11)$$

$$_yK^+ + 1e^- + V^VOPO_4 \xrightarrow{\text{Intercalation}} K_{x+y}VOPO_4 \bullet 1.5H_2O \quad (12)$$

It is important to note that recent reports indicate that water molecules play a key role in the intercalation process and not only stabilize the lamellar structure. The authors argue that the presence of water in the electroactive material is essential to achieve a reversible process with long term cycling [60]. Additionally, it has been recently recognized that the presence of water molecules in the tunnels of the crystalline structures 1D [10] and 2D [61] allows the insertion of electrolyte ions, like OH^- and H^+, increasing the rate of charge-discharge and stability upon cycling.

In Figure 5 is shown the percentage of capacitance retention as a function of cycle number for $VOPO_4 \bullet 2H_2O$ in three different aqueous electrolytes. The electrochemical window is 1.0 V in alkaline electrolytes and 1.1 V in neutral electrolyte. In all the cases, the percentage of capacitance retention is above 90 % after 5000 cycles of charge discharge at the scan rate of 100 mVs^{-1}. This is an impressive stable behavior not often reported in the literature. For instead, the VN

[59], VN_xO_y or V_2O_5 [61] analogues of these vanadium phosphates are not very stable upon cycling, even with a narrow electrochemical window. Thus, the large electrochemical window in aqueous electrolytes, high rates of charge and discharge and long-term cycling stability are related to the chemical composition, phosphate groups, crystalline water molecules and crystalline structure with 2D tunnels. This layered vanadium phosphate appears as a good candidate for real-life devices.

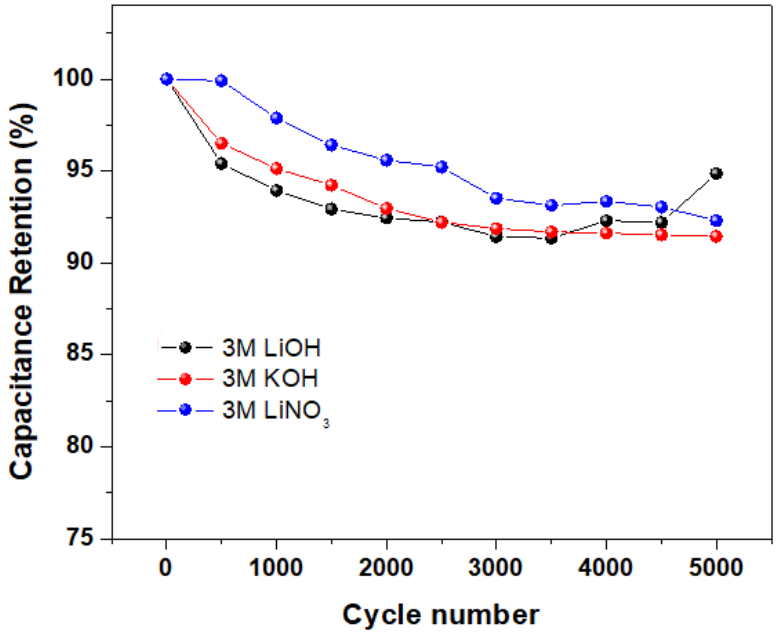

Figure 5. Capacitance retention as a function of cycle number for $VOPO_4 \cdot 2H_2O$ in different electrolytes at the scan rate of 100 mVs^{-1}.

4. Conclusions

The electrochemical behavior of $VOPO_4 \cdot 2H_2O$ was studied in three different electrolytes (3M $LiNO_3$, 3M KOH and 3M LiOH). It was observed a higher specific capacitance in alkaline electrolytes than in neutral electrolyte. $VOPO_4 \cdot 2H_2O$ showed a high specific capacitance (500 μFcm^{-2}, 70 Fg^{-1}) when 3M LiOH was used. The coupled Trasatti-Dunn method and electrochemical impedance

spectroscopy were used to show the diffusion process originated by ion intercalation into the crystalline structure. This work emphasizes the fact that when the ion intercalation takes place, the *b* values are not exactly 0.5. The reason is that the charge storage processes are coupled. With the coupled Trasatti-Dunn method, the charge arising from each mechanism was obtained. This evidences that the ion intercalation is present across the applied potential window, at high scan rates as 100 mVs^{-1} and the amount of charge from each process depends on the nature of the electrolyte. Electrochemical impedance spectroscopy also confirms the ion intercalation process into the crystalline structure in 3M LiOH. Thus, these kinds of analyses are necessary to show the ion intercalation process in electrode materials for electrochemical capacitors. Hence, $VOPO_4 \cdot 2H_2O$ shows a hybrid behavior between a supercapacitor electrode and a battery electrode due to the presence of both charge storage mechanisms of these devices.

Furthermore, $VOPO_4 \cdot 2H_2O$ is a candidate for real devices due to their stability upon cycling, high rates of charge/discharge, a large areal capacitance (500 μFcm^{-2}) and a wide electrochemical window in aqueous electrolyte in negative potentials allowing the use of these material as negative electrode in asymmetric devices. Then, the challenge is to synthesize materials with tunnels in their crystalline structure that allow fast ion intercalation with higher specific surface area in order to increase the charge storage. However, we must keep in mind that in order to take advantage and capitalize the properties of electrode materials, new methodologies of electrode assembly must be developed.

Acknowledgments

This research was supported by CONCACYT-Mexico, project number 255535. The authors also acknowledge to the Mexican CONACYT Research Network of Energy Storage.

5. References

[1] Y. Wang, Y. Song, and Y. Xia, *Chem. Soc. Rev.*, 45, 5925 (2016).

[2] P. Simon and Y. Gogotsi, *Nat. Mater.*, 7, 845 (2008).

[3] B. Conway, *Electrochemical Supercapacitors*, Kluwer Academic, New York (1999).

[4] R. Lucio Porto, R. Frappier, J.B. Ducros, C. Aucher, H. Mosqueda, S. Chenu, B. Chavillon, F. Tessier, F. Cheviré, and T. Brousse *,Electrochim. Acta*, 82, 257 (2012)

[5] V. Augustyn, P. Simon, and B. Dunn, *Energ. Environ. Sci.*, 7, 1597 (2014).

[6] X. Lang, H. Mo, X. Hu, and H. Tian, *Dalton Trans.,* 46, 13720 (2017).

[7] H. Wang, Y. Liang, T. Mirfakhrai, Z. Chen, H. S. Casalongue, and H. Dai, *Nano Res.*, 4, 729 (2011).

[8] B. Anasori, M. R. Lukatskaya, and Y. Gogotsi, *Nat. Rev. Mats.*, 2, 16098, (2017).

[9] M. Fu, W. Chen, X. Zhu, and Q. Liu*, J. Power Sources*, 396, 41, (2018).

[10] J. Zuñiga, R. Lucio Porto, I. Moreno, T. Brousse, J. Aguilar Martínez and L. López Pavón, *J. Electrochem. Soc.*, 165, 10, A2349 (2018).

[11] Z. Luo, E. Liu, T. Hu, Ionics 21, 289 (2015).

[12] J. Benziger, V. Guliants, and S. Sundaresan, *Catal. Today*, 33, 49 (1997).

[13] V. Pralong, V. Caignaert, and B. Raveau, *J. Mater. Chem.*, 21, 12188 (2011).

[14] W. Massa, O. Yakubovich, and O. Dimitrova, *Solid State Sci.*, 7, 950 (2005).

[15] M. Whittingham, Y. Song, S. Lutta, P. Zavalij, and N. Chernova, *J. Mater. Chem.*, 15, 3362 (2005).

[16] C. Ling, R. Zhang, and F. Mizuno, *J. Mater. Chem. A*, 2, 31, 12330 (2014)

[17] Z. Chen, Q. Chen, H. Wang, R. Zhang, H. Zhou, L. Chen, M. S. Whittingham, *Electrochem. Commun.*, 46, 67 (2014).

[18] Y. Zhang, X. J. Zhang, Q. Tang, D. H. Wu, and Z. Zhou*, J. Alloys Compd.,* 522, 167 (2012).

[19] Z. Chen , Q. Chen, L. Chen, R. Zhang, H. Zhou, N. A. Chernova and M. S. Whittingham, *J. Electrochem. Soc.*, 160, 10, A1777 (2013).

[20] X. Ma, W. Zhang, L. Kong, Y. Luo and L. Kang, *RSC Adv.*, 6, 46, 40077 (2016).

[21] H. Pang, Z. Yan, W. Wang, Y. Wei, X. Li, J. Li, J. Chen, J. Zhang, and H. Zheng, *Int. J. Electrochem. Sci.*, 7, 12340 (2012).

[22] H. Li, H. Yu, J. Zhai, L. Sun, H. Yang, S. Xie, *Mater. Lett.*, 152, 25 (2015).

[23] N. Chen, J. Zhou, Q. Kang, H. Ji, G. Zhu, Y. Zhang, S. Chen, J. Chen, X. Feng, and W. Hou, *J. Power Sources*, *344*, 185 (2017).

[24] C. Wu, X. Lu, L. Peng, K. Xu, X. Peng, J. Huang, G. Yu, and Y. Xie, *Nat. Commun.*, *4*, 1 (2013).

[25] N. Park, Kwand Kim, and Soon Ho Chang, *Electrochem. Commun*., 3, 10, 553 (2001).

[26] S. J. Lim, J. T. Vaughey, W. T. A. Harrison, L. L. Dussack, A. J. Jacobson, and J. W. Johnson, *Solid State Ionics*, 84, 3-4, 219 (1996).

[27] B. M. Azmi, T. Ishihara, H. Nishiguchi, and Y. Takita, *Electrochim. Acta*, 48, 2, 165 (2002).

[28] H. R. Tietze, Aust. J. Chem., 34, 10, 2035 (1981).

[29] G. He, W. H. Kan, and A. Manthiram, *Chem. Mater.*, *28*(2), 682 (2016).

[30] L. Peng, Y. Zhu, X. Peng, Z. Fang, W. Chu, Y. Wang, Y. Xie, Y. Li, J. J. Cha, and G. Yu, *Nano Lett.*, 17, 6273 (2017).

[31] P. Borah and A. Datta, *Appl. Catal. A-Gen.*, 376, 1, 19 (2010).

[32] A. Datta, S. Sakthivel, M. Kaur, A. M. Venezia, G. Pantaleo, and A. Longo, *Micropor. Mesopor. Mat.*, 128, 213 (2010).

[33] R. Lucio Porto, S. Bouhtiyya, J.F. Pierson, A. Morel, F. Capon, P. Boulet, and T. Brousse, *Electrochim. Acta*, 141, 203 (2014).

[34] R. Pai, A. Singh, S. Simotwo, and V. Kalra, *Adv. Eng. Mater.*, 20, 6 (2018).

[35] M. H. Alfaruqi, S. Islam, J. Gim, J. Song, S. Kim, D. Tung Pham, J. Jo, Z. Xiu, V. Mathew, and J. Kim, *Chem. Phys. Lett.*, 650, 64 (2016)

[36] T. Brousse, M. Toupin, R. Dugas, L. Athouël, O. Crosnier, and D. Bélanger, *J. Electrochem. Soc.*, 153, 12 (2006).

[37] B. Pandit, D. P. Dubal, and B. R. Sankapal, *Electrochim. Acta*, 242, 382

(2017).

[38] J. B. Mitchell, W. C. Lo, A. Genc, J. Lebeau, and V. Augustyn, *Chem. Mater.*, 29, 9, 3928 (2017).

[39] J. Tao, N. Liu, W. Ma, L. Ding, L. Li, J. Su and Y. Gao, *Sci. Rep.*, 3, 1 (2013).

[40] L. Yuan, X. Lu, X. Xiao, T. Zhai, J. Dai, F. Zhang, B. Hu, X. Wang, L. Gong, J. Chen, C. Hu, Y. Tong, J. Zhou, and Z. Lin Wang, *ACS Nano*, 6, 1, 656 (2012).

[41] T. Brousse, D. Bélanger, and J. W. Long, *J. Electrochem. Soc.*, 162, 5, A5185 (2015).

[42] S. Bouhtiyya, R. L. Porto, B. Laïk, P. Boulet, F. Capon, J.P. Pereira-Ramos, T. Brousse, J.F. Pierson, *Scr. Mater.*, 68, 659 (2013).

[43] C. Zhong, Y. Deng, W. Hu, J. Qiao, L. Zhang, and J. Zhang, *Chem. Soc. Rev.*, 44, 21, 7484 (2015).

[44] S. Trasatti, *J. Electroanal. Chem.,* 123, 121 (1981).

[45] M. Jeong, K. Zhuo, S. Cherevko, W. Kim, C. Chung, *J. Power Sources*. 244,806, (2013).

[46] Y. Zhang, Y. Zhang, H. Feng, X. Wu, L. Wang, A. Zhang, T. Xia, H. Dong, X. Li, and L. Zhang, *Int. J. Hydrogen Energ.*, 34, 4889 (2009).

[47] Y. Zhu, L. Peng, D. Chen, and G. Yu, *Nano Lett.*, 16, 1, 742 (2016).

[48] H. Lindström, S. Södergren, A. Solbrand, H. Rensmo, J. Hjelm, A. Hagfeldt, and S. Lindquist, *J. Phys. Chem. B*, 101, 7717 (1997).

[49] J. Wang, J. Polleux, J. Lim, and B. Dunn, *J. Phys. Chem. C*, 111, 14925 (2007).

[50] T. Brezesinski, J. Wang, J. Polleux, B. Dunn, and S. Tolbert, *J. Am. Chem. Soc.*, 131, 1802 (2009).

[51] S. Ardizzone, G. Fregonara and S. Trasatti. “Inner and Outer active surface of RuO2 electrodes. Electrochemical Acta, 35 , 263, (1990).

[52] Torsten Brezesinski, John Wang, Julien Polleux, Bruce Dunn and Sara H. Tolbert. J. Am. Chem. Soc. 131, 1802-1809, (2009).

[53] J. W. Lim, J. T. Vaughey, W.T.A. Harrison, L.L. Dussack, A.J. Jacobson,

Johnson, *Solid State Ionics*, 84, 3, 219 (1996).

[54] M.D. Levi, D. Aurbach, *J. Phys. Chem. B*. 101, 4630-4640, (1997)

[55] D. Aurbach, M. D. Levi, E. Levi, H. Teller, B. Markovsky, G. Salitra, U. Heider, and L. Heider, *J. Electrochem. Soc.*, 145, 9, 3024 (1998).

[56] M.D. Levi, K. Gamolsky, D. Aurbach, U. Heider, R. Oesten, *Electrochim. Acta.*, 45, 1781-1789, (2000).

[57] B. A. Boukamp, H.J.M. Bouwmeester*, Solid State Ionics,* 157, 29-33, (2003)

[58] M.D. Levi, H. Gizbar, E. Lancry, Y. Gofer. Levi D. Aurbach, *J. Electroanal. Chem.* 569, 211-223, (2004).

[59] V.S. Muralidharan, *Anti-Corros. Method. M.*, 44, 1, 26, (1997)

[60] J. Hyoung, J. W. Heo, M. S. Chae, and S. Hong, *ChemSusChem.,* 12, 1069-1075 (2019).

[61] J. B. Mitchell, W.C. Lo, A. Genc, J. LeBeau, V. Augustyn, *Chem. Mater.*, 29, 3928-3937, (2017).